

# Localized inter-valley defect excitons as single-photon emitters in WSe<sub>2</sub>

Lukas Linhart,<sup>1</sup> Matthias Paur,<sup>2</sup> Valerie Smejkal,<sup>1</sup> Joachim Burgdörfer,<sup>1</sup> Thomas Mueller,<sup>2</sup> and Florian Libisch<sup>1</sup>

<sup>1</sup>*Institute for Theoretical Physics, Vienna University of Technology, 1040 Vienna, Austria, EU.*

<sup>2</sup>*Institute of Photonics, Vienna University of Technology, 1040 Vienna, Austria, EU.*

Single-photon emitters play a key role in present and emerging quantum technologies. Several recent measurements have established monolayer WSe<sub>2</sub> as a promising candidate for a reliable single photon source. The origin and underlying microscopic processes have remained, however, largely elusive. We present a multi-scale tight-binding simulation for the optical spectra of WSe<sub>2</sub> under non-uniform strain and in the presence of point defects employing the Bethe-Salpeter equation. Strain locally shifts excitonic energy levels into the band gap where they overlap with localized intra-gap defect states. The resulting hybridization allows for efficient filling and subsequent radiative decay of the defect states. We identify inter-valley defect excitonic states as the likely candidate for anti-bunched single-photon emission. This proposed scenario is shown to account for a large variety of experimental observations including brightness, radiative transition rates, the variation of the excitonic energy with applied magnetic and electric fields as well as the variation of the polarization of the emitted photon with the magnetic field.

Transition Metal Dichalcogenides (TMDs) have attracted considerable interest over the last decade. A direct band gap in the mono layer case [1, 2], extremely large excitonic binding energies in the order of 300-500 meV [3, 5, 11] and valley as well as spin selective optical transitions due to the D<sub>3h</sub> symmetry make these materials very promising candidates for optical devices [6, 7]. Single photon emitters (SPEs) in WSe<sub>2</sub> are among the most intriguing candidates for such future optical applications attracting considerable attention in the field of two-dimensional materials [12–28]. Single-photon emitters promising photon emission “on demand” are key building blocks for optoelectronic and photonic-based quantum-technological devices, e.g., for generating entangled photons [26].

SPEs in WSe<sub>2</sub> emit antibunched light from highly localized spots in suspended WSe<sub>2</sub> flakes featuring a narrow linewidth (down to 100  $\mu\text{eV}$ ) and an intricate fine structure (for a review see [27]). A large number of experimental investigations have provided key insight to help unraveling the puzzle of the microscopic origin of SPEs. The prominent observation of SPEs in regions of enhanced strain, for example close to pillars suspending the WSe<sub>2</sub> membrane [19–21, 25], points to the crucial role of locally non-uniform strain. The large defect density in WSe<sub>2</sub> also seems to play a role in the formation of SPEs [21]. The appearance of doublets in the optical spectra – i.e., single photon emission lines with energy spacing up to 1 meV – has been attributed to the exchange interaction between excitons but the underlying mechanism has remained an open question. While in some early studies few SPEs were found to be only weakly dependent on the magnetic field, in most measurements an unexpectedly large effective g-factor ranging from 8 to 13 was observed [13–15, 17, 23, 24, 28]. Several groups observed bi-exciton doublets with a zero field splitting in the range of 0.2 to 1 meV [13–18, 20, 24–27]. For SPEs emitting from the same region, measurements find correlated polarizations, some preferentially

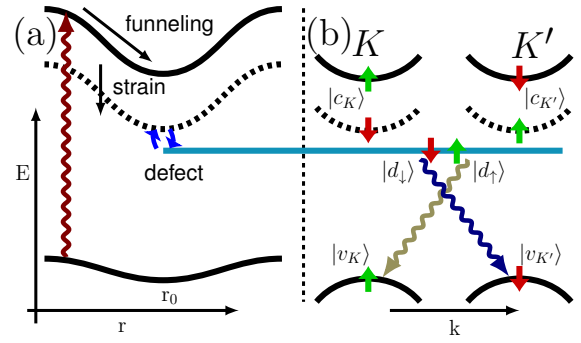


FIG. 1. Single photon emitter in WSe<sub>2</sub>, schematically (a) Real space representation: a free exciton is created (dark red arrow), strain efficiently funnels excitons with the electron in the bright (solid black line) and dark (dashed line) conduction band state down in energy towards the strain maximum near  $r_0$  due to the strain-dependent bandgap: mixing of the strain-localized dark exciton with a defect state leads to the formation of a strongly localized defect exciton. (b) Reciprocal space: while strain-localized exciton states (dashed) remain dark, a point defect (horizontal cyan line) breaks the valley selectivity and leads to efficient photoemission (dark blue/yellow arrows).

parallel to each other [14, 16, 27], while others feature pairs with orthogonal polarization, in particular for doublets [14, 17, 18, 26, 27]. Equally puzzling, both linear and quadratic Stark shifts with applied electric field were recently found for different SPEs [18, 22, 28]. On an even more fundamental level, there is no clear picture as to why a SPE in such a nanostructure possesses a brightness large enough to be measured at all. The latter suggests a remarkably large optical transition rate of the emitting state and a highly efficient repopulation subsequent to the photon emission.

A detailed microscopic model of the processes involved has remained elusive. In this letter we present a multi-scale simulation for WSe<sub>2</sub> with locally varying strain and in the presence of point defects. We em-

ploy a tight-binding model for the electronic structure on a single-particle level and a Bethe-Salpeter approach to account for two-particle interaction effects. From this simulation the following microscopic scenario for the origin of SPEs emerges: strongly non-uniform strain variations (e.g. near the tip of pillars [20]) result in the lowering of excitonic energies in the strained region [28] forming a weakly localized exciton [Fig. 1(a)]. In the presence of a point defect in this region, hybridization with a strongly localized defect level in the band gap leads to the formation of a novel electron-hole pair configuration termed inter-valley defect exciton for which the broken valley symmetry allows efficient radiative decay [Fig. 1(b)], the key prerequisite for a SPE. Within this scenario we are able to quantitatively reproduce measurements of the SPE fine structure, magnetic- and electric-field behavior as well as the polarization of the emitted light. The present simulation provides the theoretical underpinning of previously suggested qualitative models [20] and a consistent guide through a diverse array of seemingly contradictory observations.

The starting point of our description on the single-particle level is a multi-scale approach employing density functional theory (DFT) calculations [1, 2] to determine the input parameters of a subsequent tight-binding simulation of large (30 000 atoms) non-uniformly strained  $\text{WSe}_2$  crystals. This approach circumvents the need for fitting parameters by projecting onto Wannier orbitals [3, 4] at different strain amplitudes, and interpolating the tight-binding interactions for locally varying strain configurations [for details see the supplementary material (SM)]. The resulting single-particle eigenstates feature, indeed, the lowest conduction band states  $|c\rangle$  and, consequently, also the corresponding excitonic states to be localized near the local maximum of the strain amplitude [Fig. 2(a) and SM]. The larger the strain, the more deeply the states get trapped near the center of the strain pattern [Fig. 2(c)]. We find  $s$ -like radially symmetric conduction ( $|c\rangle$ ) and valence ( $|v\rangle$ ) states that are two fold (valley) degenerate [Fig. 2(a)]. The spatial variation of the energy of the conduction band and excitonic states [Fig. 1(a)] due to strain suggests the “funneling” of conduction band occupation into these strain-localized excitonic states [20]. The present results are found to be largely independent of the details of the strain pattern as long as the local variation of strain is sufficiently smooth such that intervalley scattering remains negligible. The highest-lying valence states are spin-polarized  $\langle v_K | \uparrow \rangle \approx 1$  and largely consist of atomic tungsten  $d_{x^2-y^2}$  and  $d_{xy}$  orbitals while the lowest-lying spin-polarized conduction band states  $\langle c_K | \downarrow \rangle \approx 1$  are spanned by tungsten  $d_{z^2}$  orbitals [33]. These states can be clearly associated with a well-defined valley quantum number, showing that the valley symmetry is preserved for these states under strain. Our model thus reproduces the well-known spin-valley lock-

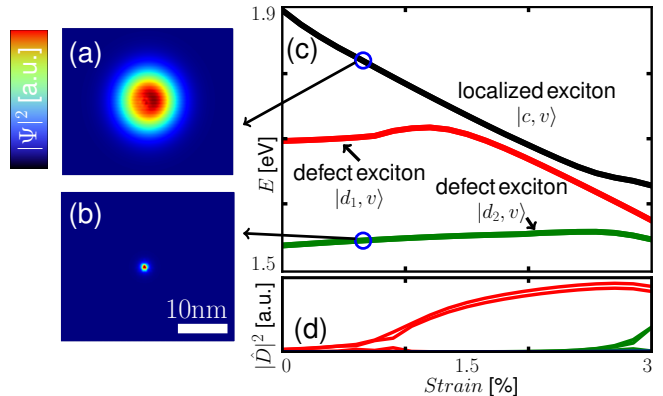


FIG. 2. Wave function and energies of strain-localized states within a single-particle picture: (a) and (b): Real space representation of a localized conduction band state  $|c\rangle$  and strongly localized vacancy defect state  $|d\rangle$ . (c) energy shift and mixing between localized exciton  $|c, v\rangle$  and defect excitons  $|d_1, v\rangle$  (red) and  $|d_2, v\rangle$  (green) as a function of strain. (d) Optical oscillation strength of excitonic states as function of strain. When  $|c, v\rangle$  and  $|d_i, v\rangle$ ,  $i = 1, 2$ , approach each other the  $|d_i, v\rangle$  exciton becomes bright. Each defect exciton spans a  $4 \times 4$  subspace [Eq. (1b)] with two optically active transitions (double lines).

ing in TMDs [5]. Spin-valley locking strongly influences the optical properties of  $\text{WSe}_2$ : in contrast to molybdenum based TMDs, the exciton in  $\text{WSe}_2$  is “dark” since optical intra-valley transitions are spin forbidden, with the spin allowed transition several tens of meV higher in energy, while inter-valley transitions (e.g.,  $K \rightarrow K'$ ) are valley forbidden [36] [Fig. 1(b)]. Consequently, direct optical transition from the excitonic to the ground state are blocked, raising intriguing questions as to the origin of the observed strong single-photon emission.

Unraveling the spin-valley locking by a local symmetry breaking through the ubiquitous presence of defects appears key to understanding and describing SPEs in  $\text{WSe}_2$ . We therefore include in our simulations simple prototypical point defects, specifically either a single or a double Se vacancy. While both break the in-plane translational symmetry, single Se vacancies also break the out-of plane inversion symmetry while the latter is preserved by the double vacancy. The simulation yields a strongly localized defect state  $|d\rangle$  [Fig. 2(b)], with energy below the conduction band, i.e., an electron-like state at normal doping [Fig. 2(c)]. It features two spin states ( $|d_\uparrow\rangle, |d_\downarrow\rangle$ ), but no well-defined valley polarization due to its strong localization. While also other specific defect types have been proposed as possible origins of SPEs [28, 34, 35], we note that the presence of any valley symmetry breaking defect seems sufficient, as long as it results in a localized state near the defect site energetically close enough to the bottom of the bulk conduction band to allow hybridization due to strain [Fig. 1(a)].

The present one-particle description of a WSe<sub>2</sub> monolayer crystal that is locally strained and decorated with a point defect is now the starting point for inclusion of two-particle interactions. For the solution of the Bethe-Salpeter equation (BSE) [37] we employ our one-particle wave functions to form a particle-hole basis  $|c_j, v_i\rangle = |c\rangle^e \oplus |v\rangle^h$ , with particle state  $|c_j\rangle$  and hole state  $|v_i\rangle$ , where the index  $(i, j)$  refers to the valleys  $(K, K')$  the states are associated with. Since the excitonic states of interest are energetically well separated from the conduction and valence band continua and spatially localized, we restrict ourselves to the two-particle space spanned by,

$$\{|c_K v_K\rangle, |c_{K'} v_K\rangle, |c_K v_{K'}\rangle, |c_{K'} v_{K'}\rangle\} \quad (1a)$$

and furthermore include defect excitons

$$\{|d_\uparrow v_K\rangle, |d_\downarrow v_K\rangle, |d_\uparrow v_{K'}\rangle, |d_\downarrow v_{K'}\rangle\}. \quad (1b)$$

We solve the BSE-type equation

$$\mathcal{H}^{\text{tp}}|c_i, v_j\rangle = \mathcal{E}|c_i, v_j\rangle, \quad \mathcal{H}^{\text{tp}} = (\epsilon_{c_i} - \epsilon_{v_j})\delta_{i'}^i \delta_{j'}^j + \Xi_{c_i, v_j}^{c_i', v_j'} \quad (2)$$

where  $\Xi_{c_i, v_j}^{c_i', v_j'} = W_{c_i, v_j}^{c_i', v_j'} - V_{c_i, v_j}^{c_i', v_j'}$  is the BSE interaction kernel,  $W$  is the direct part and  $V$  the indirect contribution [10] (for details, see SM). The direct part  $W$  of the two-particle interaction shifts the states downwards in energy by  $\approx 100 - 500$  meV depending on the value chosen for the dielectric constant (we use  $\epsilon/\epsilon_0 = 10$  in the following [40]). Shifts of this order of magnitude are consistent with experimentally observed excitonic binding energies. While the indirect contribution  $V$  is at least two orders of magnitude smaller, it is key to understand the fine-structure of SPE spectra. The direct term  $W$  does not lift the degeneracy since spin/valley locking allows only for non-vanishing Hartree-like diagonal terms. In the absence of defects, spin/valley locking prohibits also any non-vanishing off-diagonal contributions for  $V$  for strain-localized excitonic states  $\{|c, v\rangle\}$  (In contrast to bright A-excitons [39]). Only in the presence of defects with particle-hole states  $\{|d, v\rangle\}$  off-diagonal contributions and, thus, fine-structure splittings of the excitonic states (as observed in experiment) arise. The following scenario for bright excitons emerges: diagonalizing the BSE Hamiltonian [Eq. (2)] in the subspace of Eq. (1b) thereby neglecting the hybridization between the defect state and the conduction band yields localized inter-valley defect excitonic (IDE) states approximated by

$$|\text{IDE}_\pm\rangle \approx \frac{1}{\sqrt{2}} \left( |d_{\uparrow(\downarrow)} v_{K(K')}\rangle \pm |d_{\downarrow(\uparrow)} v_{K'(K)}\rangle \right), \quad (3)$$

these IDE states appear in doublets ( $\pm$ ) with an energy splitting of  $\Delta_0 \approx 0.8 - 2$  meV, well in the experimentally observed range. Thus, the defect breaking the valley symmetry leads to the formation of doublets [Eq. (S13)]

with an energy spacing given by the exchange splitting. We note that inclusion of the hybridization of defect states with the conduction band by diagonalization of the BSE Hamiltonian in the full  $8 \times 8$  space [Eq. (1)] can give rise to pairs of coupled doublets, possibly accounting for recent observations [17, 27] (see SM).

The IDE excitons [Eq. (S13)] are efficiently populated by the locally varying strain that shifts free “bulk” excitonic states  $|c, v\rangle$  in energy towards defect excitonic states  $|d, v\rangle$  [Fig. 1] thereby effectively funneling population into IDEs. Most importantly, the formation of defect excitons is accompanied by a dramatic increase in optical transition strength (or reduction in radiative lifetimes) when  $|c, v\rangle$  and  $|d, v\rangle$  approach each other in energy [Fig. 2 (d)]. While the transition strength of “bulk” excitons  $|c, v\rangle$ , even in the presence of strain, is of the order of  $10^7 \text{ s}^{-1}$  and thus too small to serve as efficient photon emitter, the hybridization with the defect state, which breaks the valley locking, increases the transition strength by about two orders of magnitude to  $10^9 \text{ s}^{-1}$ . The corresponding radiative lifetime, which is of the order of nanoseconds, is in good agreement with experiment. These predictions are robust against variations of the defect model or the strain pattern. In turn, spatially separating the defect from the strained region decreases the transition rate as the overlap between strain-localized excitons  $|c, v\rangle$  and the excitonic defect state  $|d, v\rangle$  decreases.

The present model of localized IDE states as source of SPEs allows to make detailed predictions for the response, both in energetic position and polarization to magnetic and electric fields without resorting to any adjustable parameter.

With increasing magnetic field perpendicular to the crystal (Faraday configuration) the zero-field exciton formed near a Se vacancy defect undergoes a well known pronounced avoided crossing [Fig. 3(b)] with splitting  $\Delta(B) = \sqrt{\Delta_0^2 + (\mu_0 g_{\text{eff}} B)^2}$  and  $\Delta_0$  the zero-field splitting of the IDE doublet [Eq. (S13)], in excellent agreement with several measurements of the magnetic field evolution of SPE doublets [13–16, 18, 20, 21, 24–28]. The linearly polarized exciton at  $B = 0$  [right-handed ( $\sigma^+$ ) and left-handed ( $\sigma^-$ ) emission being equal] approaches circular polarization with increasing magnetic field [Fig. 3(c,d)] as for the free exciton [5]. Above  $\approx 2$  T these high-field excitons can again be associated with well defined valley quantum numbers. In the high-field regime the magnetic response becomes linear controlled by the orbital magnetic moment of the valence (conduction) band states near the  $K(K')$  points  $\mu \pm 4.4\mu_0$  ( $\pm 3.5\mu_0$ ) for  $|v_{K(K')}\rangle$  with opposite signal for the two valleys, as they are connected by time reversal symmetry (similar to [41]). By contrast, a defect strongly localizes on a few atomic sites and hardly contributes to the shift with magnetic field. Therefore, the defect exciton with an effective  $g$ -factor of  $g_{\text{eff}} = 2 \cdot 4.4 = 8.8$

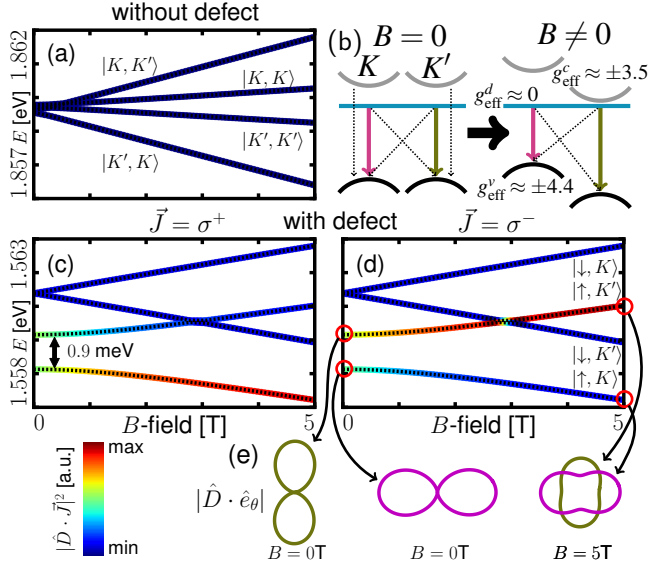


FIG. 3. Magnetic field dependence of energy and polarization of localized excitons. (a) without a defect. (b) Schematic illustration of possible transitions and the calculated effective g-factor of single particle states. All transitions are dark (dashed arrows) for the defect free case, while IDEs are optically active (colored arrows). Simple Zeeman splitting of  $|c_{K(K')} \rangle$  and  $|v_{K(K')} \rangle$  in the absence of strain, together with the corresponding effective g-factors. (c)-(d) double Se vacancy (see SM for single vacancy). (c) right-handed [(d): left-handed] circularly polarized emission  $\sigma^+$  [ $\sigma^-$ ] as function of magnetic field. Color-scheme of the line marks the intensity of the transition by projection on the corresponding polarization vector  $\vec{J} = \sigma^+$  [ $\vec{J} = \sigma^-$ ]. (e) Polar plot of the linear polarization of the emitted light as function of polarization angle.

displays a much smaller (larger) Zeeman shift than the bulk inter-valley exciton  $|c_K, v_{K'} \rangle$  (intra-valley excitons  $|c_K, v_K \rangle$ ) with an  $g_{\text{eff}} = 2 \cdot (4.4 + 3.5) = 15.8$  ( $g_{\text{eff}} = 2 \cdot (4.4 - 3.5) = 1.8$ ) [see Fig. 3 (a,b)]. A g-factor of 15.8 was recently reported for localized states in valley-aligned TMD heterobilayers [42], further underpinning our calculations.

We could not yet identify a systematic pattern that would connect the polarization axis with the lattice orientation or the strain gradient. However, our model allows for defining predictions for the correlation between the polarization axes of SPEs residing in close spatial proximity on the flake: the two lines from the doublet ( $\text{IDE}_\pm$ ) have polarization axes orthogonal to each other [Fig. 3(e)] while excitons stemming from different inter-gap states of one single defect feature linear polarization with the polarization axis parallel to each other, as the lattice distortions (and therefore the relative weights of the dipole matrix elements) are similar. These results suggest an explanation for the seemingly contradicting measurements regarding either parallel or orthogonal relative linear polarizations of spatially close

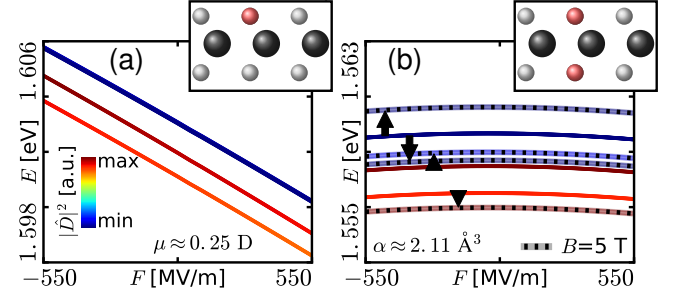


FIG. 4. Stark shift of SPE. (a) For a single Se vacancy (inversion symmetry breaking defect). (inset) side view of the WSe<sub>2</sub> layer with a vacancy (red). Color scheme as in Fig. 3 (b) For a double Se vacancy (symmetry preserving) defect, dashed lines are calculated with an additional magnetic field (5T). Black arrows indicate the evolution of each state with magnetic field.

SPE peaks.

Turning now to the dielectric response to an external electric field  $F$  oriented perpendicular to the plane of the WSe<sub>2</sub> crystal, a wide array of different experimental results have been reported. Parametrizing the energy shift of the SPE as  $E = E_0 - \mu_F F - \frac{1}{2} \alpha F^2$  with  $\mu_F$  the electric dipole moment and  $\alpha$  the polarizability, both linear and quadratic Stark shifts have been observed with  $\mu_F$  ranging from 0.05 to 10 Debye and  $\alpha$  from 0.1 to 1000  $\text{\AA}^3$  [18, 22, 28]. The two prototypical point defects treated by our model, the single Se vacancy breaking the out-of plane inversion symmetry and the double Se vacancy preserving this symmetry, pinpoint the origin of such diverse results. With the out-of-plane inversion symmetry broken by a single Se vacancy, we find a pronounced linear Stark shift with  $\mu_F = 0.25$  D [Fig. 4 (a)]. For a double vacancy we observe only a quadratic Stark effect with  $\alpha = 2.1 \text{\AA}^3$  [Fig. 4]. Our results fit well to a linear-response model which estimates the Stark shift based on the density difference in the top and bottom Se layer. For the present single Se vacancy the density asymmetry is about 1%, in principal allowing  $\mu_F$  to be up to two orders of magnitude larger, well within the experimental range.

In summary, we have developed a microscopic model for bright single photon emitters in WSe<sub>2</sub> and have identified inter-valley defect excitons as likely candidates for strong photoemission. The interplay between strain and point defects allows to effectively funnel bulk excitons near the  $K(K')$  point into localized defect excitons. The broken lattice symmetry by the point defect breaks the spin-valley locking thereby opening the door to a large optical transition strength, a key prerequisite for bright photon emission. The broken valley symmetry also gives rise to an inter-valley mixture of the defect exciton, explaining the splitting in doublets at zero magnetic field. The predicted dielectric and paramagnetic response of

the inter-valley localized defect excitons is consistent with a large number of experimental observations. The model is also capable of predicting the variation of the polarization of the SPE photons with applied magnetic field. Some intriguing questions, however, remain open. Among them are the statistics of energy and brightness fluctuations of the SPE, the conclusive identification of the dominant defect type, and the kinetics of the repopulation by the funnel. Addressing these questions is key to controlling single photon emission from WSe<sub>2</sub> for quantum optics and quantum information applications.

We acknowledge support by the TU-D doctoral program of TU Wien, as well as from the Austrian Science Fund (FWF), project I-3827.

- 
- [1] K.F. Mak, C. Lee, J. Hone, J. Shan and T. F. Heinz, , Phys. Rev. Lett. **105**, 136805, (2010).
- [2] A. Splendiani, L. Sun, Y. Zhang, T. Li, J. Kim, C. Chim, G. Galli and F. Wang, , Nano Lett., **10** (4), pp 1271-1275, (2010).
- [3] A. Chernikov, T.C. Berkelbach, H. M. Hill, A. Rigosi, Y. Li, O. B. Aslan, D. R. Reichman, M. S. Hybertsen and T. F. Heinz, , Phys. Rev. Lett. **113**, 076802, (2014).
- [4] K. He, N. Kumar, L. Zhao, Z. Wang, K. F. Mak, H. Zhao and J. Shan, , Phys. Rev. Lett. **113**, 026803, (2014).
- [5] T. Cao, G. Wang, W. Han, H. Ye, C. Zhu, J. Shi, Q. Niu, P. Tan, E. Wang, B. Liu and J. Feng, Nature Comm. **3**, 887, (2012).
- [6] T. Mueller and E. Malic, 2D Mat. and App. **2**, 29, (2018).
- [7] G. Wang, A. Chernikov, M. M. Glazov, T. F. Heinz, X. Marie, T. Amand and B. Urbaszek, Rev. Mod. Phys. **90**, 021001, (2018).
- [8] P. Tonndorf, R. Schmidt, R. Schneider, J. Kern, M. Buscema, G. A. Steele, A. Castellanos-Gomez, H. S. J. van der Zant, S. Michaelis de Vasconcellos and R. Bratschitsch, Optica **2**, 347-352, (2015).
- [9] S. Kumar, A. Kaczmarczyk and B. D. Gerardot, Nano Lett. **15**, 7567-7573, (2015).
- [10] Y. He, G. Clark, J. R. Schaibley, Y. He, M. Chen, Y. Wei, X. Ding, Q. Zhang, W. Yao, X. Xu, C. Lu and J. Pan, Nature Nano. **10**, 497-502, (2015).
- [11] A. Srivastava, M. Sidler, A. V. Allain, D. S. Lembke, A. Kis and A. Imamoglu, Nature Nano. **10**, 491-496, (2015).
- [12] S. Kumar, M. Brotóns-Gisbert, R. Al-Khuzheyri, A. Branny, G. Ballesteros-Garcia, J. F. Sánchez-Royo and B. D. Gerardot, Optica **3**, 882-886, (2016).
- [13] S. Schwarz, A. Kozikov, F. Withers, J. K. Maguire, A. P. Foster, S. Dufferwiel, L. Hague, M. N. Makhonin, L. R. Wilson, A. K. Geim, K. S. Novoselov and A. I. Tartakovskii, 2D Mater. **3**, 025038, (2016).
- [14] C. Palacios-Berraquero, M. Barbone, D. M. Kara, X. Chen, I. Goykhman, D. Yoon, A. K. Ott, J. Beitner, K. Watanabe, T. Taniguchi, A. C. Ferrari and M. Atatüre, Nature Comm. **7**, 12978, (2016).
- [15] J. Kern, I. Niehues, P. Tonndorf, R. Schmidt, D. Wigger, R. Schneider, T. Stiehm, S. Michaelis de Vasconcellos, D. E. Reiter, T. Kuhn and R. Bratschitsch, Adv. Mater. **28**, 7101-7105, (2016).
- [16] A. Branny, S. Kumar, R. Proux and B. D. Gerardot, Nature Comm. **8**, 15053, (2017).
- [17] Y. Luo, G. D. Shepard, J. V. Ardelean, D. A. Rhodes, B. Kim, K. Barmak, J. C. Hone and S. Strauf, Nature Nano. **13**, 1137-1142, (2018).
- [18] C. Chakraborty, N. R. Jungwirth, G. D. Fuchs and A. N. Vamivakas, Phys. Rev. B, **99**, 045308, (2019).
- [19] X. Lu, X. Chen, S. Dubey, Q. Yao, W. Li, X. Wang, Q. Xiong and A. Srivastava, Nature Nano. DOI:10.1038/s41565-019-0394-1 (2019).
- [20] M. Koperski, K. Nogajewski, A. Arora, V. Cherkez, P. Mallet, J.-Y. Veuillen, J. Marcus, P. Kossacki and M. Potemski, Nature Nano. **10**, 503-506, (2015).
- [21] C. Chakraborty, L. Kinnischtzke, K. M. Goodfellow, R. Beams and A. N. Vamivakas, Nature Nano. **10**, 507-511, (2015).
- [22] C. Palacios-Berraquero, D. M. Kara, A. R.-P. Montblanch, M. Barbone, P. Latawiec, D. Yoon, A. K. Ott, M. Loncar, A. C. Ferrari and M. Atatüre, Nature Comm. **8**, 15093, (2017).
- [23] G. Clark, J. R. Schaibley, J. Ross, T. Taniguchi, K. Watanabe, J. R. Hendrickson, S. Mou, W. Yao and X. Xu, Nano. Lett. **16**, 3944-3948, (2016).
- [24] Y. He, O. Iff, N. Lundt, V. Baumann, M. Davanco, K. Srinivasan, S. Höfling and C. Schneider, Nature Comm. **7**, 13409, (2016).
- [25] C. Chakraborty, K. M. Goodfellow, S. Dhara, A. Yoshimura, V. Meunier and A. N. Vamivakas, Nano. Lett. **17**, 2253-2258, (2017).
- [26] D. Huber, M. Reindl, Y. Huo, H. Huang, J. S. Wildmann, O. G. Schmidt, A. Rastelli and R. Trotta, Nature Comm. **8**, 15506, (2017).
- [27] M. Koperski, M. R. Molas, A. Arora, K. Nogajewski, A. O. Slobodeniuk, C. Faugeras and M. Potemski, Nanophotonics **6**, 1289-1308, (2017).
- [28] S. B. Desai, G. Seol, J. S. Kang, H. Fang, C. Battaglia, R. Kapadia, J. W. Ager, J. Guo and A. Javey, Nano Lett., **14**, 4592-4597, (2014).
- [29] G. Kresse and J. Hafner, Phys. Rev. B **47**, 558-561, (1993).
- [30] G. Kresse and J. Hafner, Phys. Rev. B **49**, 251-271, (1994).
- [31] N. Marzari and D. Vanderbilt, Phys. Rev. B **56**, 847-865, (1997).
- [32] I. Souza, N. Marzari and D. Vanderbilt, Phys. Rev. B **65**, 035109, (2001).
- [33] E. Cappelluti, R. Roldán, J.A. Silva-Guillén, P. Ordejón and F. Guinea, Phys. Rev. B, **88**, 075409, (2013).
- [34] S. Zhang, C. Wang, M. Li, D. Huang, L. Li, W. Ji and S. Wu, Phys. Rev. Lett. **119**, 046101, (2017).
- [35] Y. Zheng, Y. Chen, Y. Huang, P. K. Gogoi, M. Y. Li, L. Li, P. E. Trevisanutto, Q. Wang, S. J. Pennycook, A. T. Wee and S. Y. Quek, arxiv. 1811.00221, (2018).
- [36] J. P. Echeverry, B. Urbaszek, T. Amand, X. Marie and I. C. Gerber Phys. Rev. B, **93**, 121107, (2016).
- [37] E. E. Salpeter and H. A. Bethe, Phys. Rev. **84**, 1232, (1951).
- [38] L. Reining in, E. Pavarini, E. Koch, J. von den Brink and G. Sawatzky, ISBN 978-3-95806-159-0, **6**, (2016).
- [39] M. M. Glazov, E. L. Ivchenko, G. Wang, T. Amand, X. Marie, B. Urbaszek and B. L. Liu, Phys. Status Solidi B **252**, 2349-2362, (2015).
- [40] A. Laturia, M. L. Van de Put and W. G. Vandenberghe,

2D Mat. and Appl. 2, **6**, (2018).

- [41] A. Srivastava, M. Sidler, A. V. Allain, D. S. Lembke, A. Kis and A. Imamoglu, Nature Physics **11**, 141-147, (2015).
- [42] K. L. Seyler, P. Rivera, H. Yu, N. P. Wilson, E. L. Ray, D. G. Mandrus, J. Yan, W. Yao and X. Xu, Nature, **567**, 66-70, (2019).

# Supplemental Materials: Localized inter-valley defect excitons as single-photon emitters in WSe<sub>2</sub>

## DFT CALCULATIONS

DFT calculations were performed using VASP [S1, S2]. We used an orthorhombic unit cell containing 6 atoms per cell, a  $k$  mesh of  $19 \times 13 \times 1$   $k$  points, 35 Å vacuum in  $z$  direction, PBE functional and a non-collinear spin polarized basis. All calculated configurations were first calculated via ionic relaxation until  $\Delta F < 10^{-7}$ . Subsequently we include uniform strain in  $x$  and  $y$  direction, with 20 configurations in each direction ranging from -2% to 2% strain.

The few highest valence bands and lowest conduction bands were then transformed into an localized basis using Wannier90 [S3, S4]. As initial projections for the Wannier orbitals we used the 4p orbitals of Se and the 5d orbitals of W, each spin polarized. While this choice of initial projection results in a rather large tight-binding basis (6 sites per Se atom and 10 sites per W atom) it resembles the orbital character of the system and therefore allows for a simple intuitive picture. The new localized basis still reaches DFT accuracy.

To allow for a more direct comparison of involved energies, a scissor operator was included in the transformation to obtain a direct band gap of 2.0 eV in the unstrained case, close to the experimentally observed electronic band gap [S11]. Including the scissor operator required small modifications to the Wannier90 code.

## NON-UNIFORM STRAIN

The DFT calculation yields hopping parameters  $\gamma_{ij}$  between all orbitals of the tight-binding basis of the WSe<sub>2</sub> lattice as a function of uniform strain amplitudes. For inclusion of non-uniform strain, each hopping parameter  $\gamma_{i,j}(\vec{r})$  between two orbitals  $i$  and  $j$  separated by  $\vec{r} = (x, y)$  is approximated by a linear expansion of their spacing relative to the relaxed configuration  $\vec{r}_0 = (x_0, y_0)$  (see [Fig. S1 (a)])

$$\gamma_{i,j}(\vec{r}) = \gamma_{i,j}^0 + (x - x_0) \frac{\partial \gamma_{i,j}}{\partial x} + (y - y_0) \frac{\partial \gamma_{i,j}}{\partial y}. \quad (\text{S1})$$

Since the overlap between neighboring orbitals decays exponentially, for small displacements ( $|\vec{r} - \vec{r}_0|/|\vec{r}_0| \lesssim 3\%$ ) a linear approximation achieves a high accuracy.

This approach has several advantages: it does not require any additional fitting parameter, it preserves the original atomic orbital and spin configuration of the system thereby allowing for a straightforward physical interpretation and it sets no restrictions on the shape of the non-uniform strain pattern. We are not aware of any other model for TMD's that can capture non-uniform strain configurations. To test this description, we compare calculated bandstructures and hopping parameters obtained from an interpolation and from a direct DFT calculation and find almost perfect agreement (see [Fig. S1 (b)-(e)]).

To simulate the localization by non-uniform strain, we use a large WSe<sub>2</sub> flake ( $38 \times 32$  nm,  $\approx 200000$  orbitals) with a Mexican-hat shaped strain pattern,

$$\mathcal{S}(\vec{r}) = \mathcal{S}_{\max} \cdot \left( 1 - \frac{|\vec{r} - \vec{r}_0|^2}{\sigma^2} \right) \cdot \exp \left\{ - \left( \frac{|\vec{r} - \vec{r}_0|}{2\sigma} \right) \right\}^2. \quad (\text{S2})$$

with the strain maximum  $\mathcal{S}_{\max}$  in the center of the flake  $\vec{r}_0$ , and  $\sigma$  one third of the geometry width [Fig. S2]. The interaction parameters between adjacent sites are now determined from our tight-binding model using Eqs. (S1) and (S2). This strain pattern is the simplest configuration that leaves the positions at the borders of the geometry unchanged, allowing to attach open boundary conditions included via self-energies of half infinite leads on all four edges of the geometry [S5, S8, S9] (see [Fig. S2]).

The single-particle eigenvalue problem can then be written as,

$$\left( \mathcal{H}_{\text{sp}} + \Sigma_{\text{L}}^{v(c)} + \Sigma_{\text{R}}^{v(c)} + \Sigma_{\text{T}}^{v(c)} + \Sigma_{\text{B}}^{v(c)} \right) \Psi = \epsilon \Psi, \quad (\text{S3})$$

where  $\Psi$  is the single particle wave function,  $\mathcal{H}_{\text{sp}}$  the single-particle Hamiltonian and the  $\Sigma$ 's are the complex self-energies accounting for the openness of the flake in all for directions  $\pm x, \pm y$ . These self-energies lead to a non-norm-conserving Hamiltonian (eigenenergies  $\in \mathbb{C}$ ), the imaginary part of the eigenenergies introduces a measure



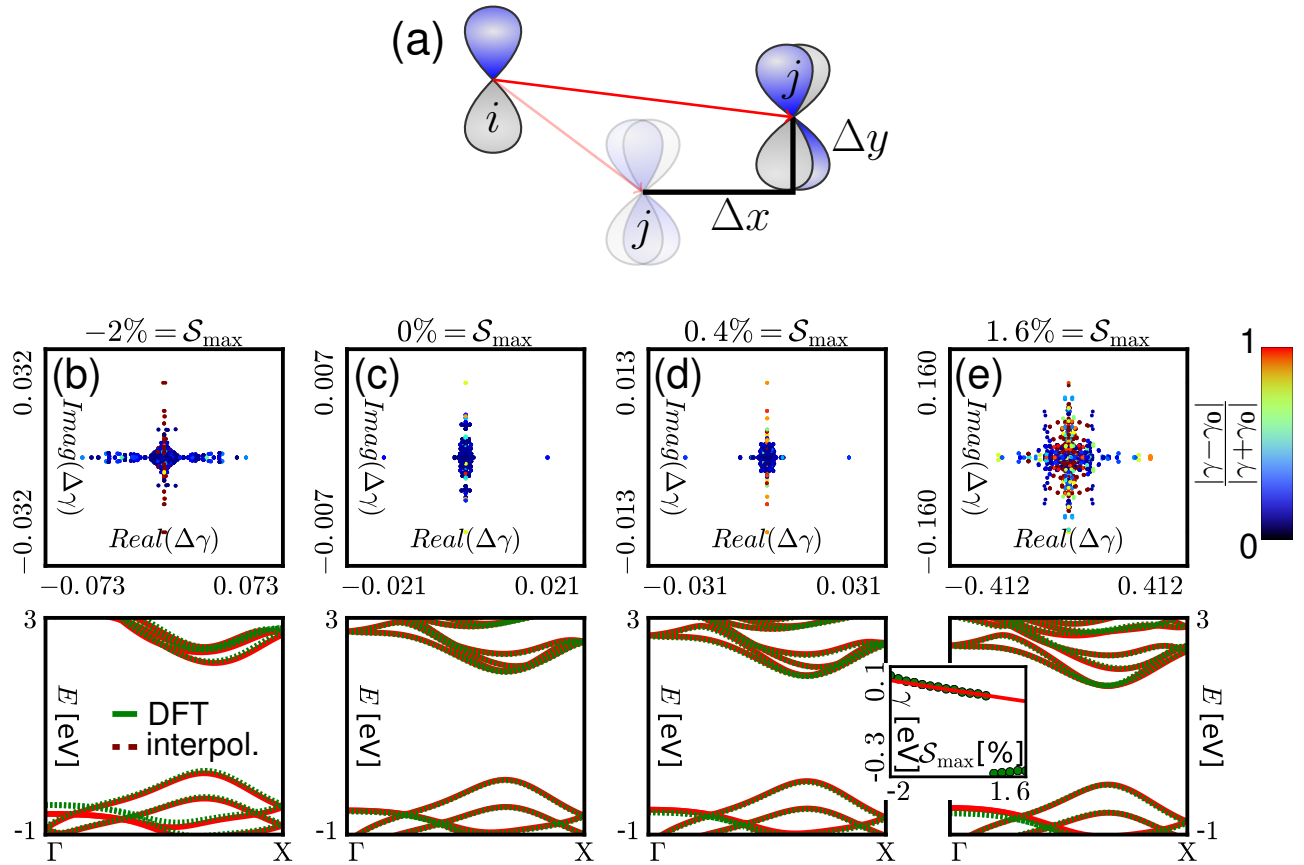


FIG. S1. Illustration of the interpolation of the interaction parameters between orbital site  $i$  and  $j$ . (a) Schematic illustration of the interpolation. (b) first row: absolute and relative error of all interaction parameters  $\gamma_{i,j}$ , between DFT calculated  $\gamma$ 's and interpolated  $\gamma$ 's, for an orthorhombic unit cell strained in  $x$  and  $y$  direction. (b) second row: comparison of band structures for different strain values. (b) inset: example of one  $\gamma$  parameter for different strain values. Green dots indicate values from the Wannierization procedure and the red line the interpolated values. For large strain values ( $\leq 1.4\%$ ) the Wannierization procedure ends up in a slightly different minimum, leading to large differences in the compared parameters. However this does not limit the accuracy of the description, as the  $\gamma$ 's of the old Wannier minima can be linearly extrapolated, still reproducing the band structure.

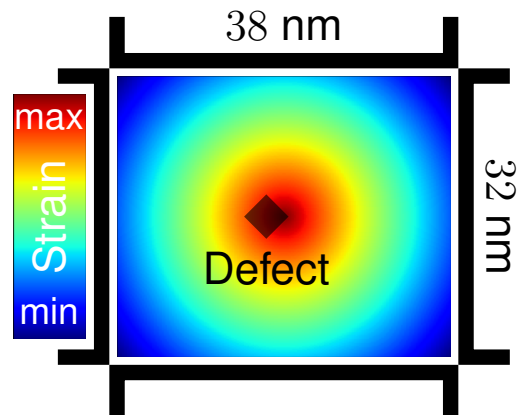


FIG. S2. Schematic illustration of the model system containing a local strain maximum and a defect site (diamond). Black lines indicate open boundary conditions calculated via the self energies of half infinite leads [S8] and expanded via a Bloch-Ansatz [S9].



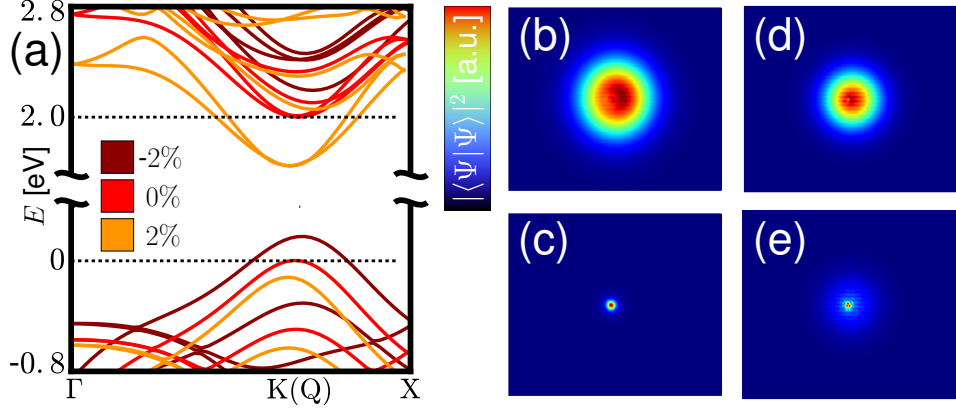


FIG. S3. (a) Calculated band structure of WSe<sub>2</sub> as a function of uniform strain. Strain is applied uniformly in  $x$ - and  $y$ -direction. For compressive strain we find WSe<sub>2</sub> to be an indirect semiconductor ( $\Gamma$ -Q transition). For tensile strain we find a lowering of the conduction band that is proportional to the applied strain, with a slope of  $\approx 140$  meV/% strain, partly compensated by the valence band with  $\approx 40$  meV/% strain. The conduction band splitting is strongly underestimated in DFT. (b) and (c) as in main text, (d) valence wave function when a localization potential is introduced, (e) defect wave function intermixed with the conduction state  $|c\rangle$  for a given strain configuration.

for the coherent dissipation of the localized wave functions into the bulk. To efficiently calculate the self-energy for edges of this size we make use of the periodicity of the non-strained edge unit cells via a Bloch Ansatz [S9]. The eigenstates  $\Psi_{c(v)}$  around the valence band maximum and the conduction band minimum are calculated using a shift-and-invert Arnoldi-Lanczos scheme [S6, S7]. The magnetic field is included via a Peierls phase [S8], defects are modeled by removing the orbitals at the defect site from the calculation geometry.

Fig. S3 (a) illustrates the evolution of the band structure as a function of uniform strain. While both band extrema move down in energy, the conduction band minimum shifts much stronger with applied strain than the valence state. Employing a non-uniform strain pattern leads to a localization of the conduction state with respect to the maximum of the strain pattern  $\vec{r}_0$  within the bandgap. The valence band does not feature a similar localization on the single particle level since the single particle states will be shifted downwards in energy away from the bulk band gap [Fig. S3 (a) valence band]. Due to a strong Coulomb interaction an excited electron-hole pair will nevertheless localize at the electron site. Since we cannot employ a self-consistent two-particle correction, we introduce a weak localizing potential in the shape of the strain pattern with a maximum energy  $U_{\max} = 80$  meV [see Eq. (S2)], far smaller than the excitonic binding energy. When introducing a localization potential  $|v\rangle$  is similar in shape to  $|c\rangle$  [Fig. S3 (right) (d)].

Qualitatively, the properties of the valence state wavefunction do not change when including such a potential. Moreover most of the quantities discussed in this paper have numerical values independent of the localization potential. Only the calculated transition rate  $w$  and the magnitude of the zero field splitting  $\Delta_0$  change without localization potential, due to the different electron-hole overlap. However the relative transition rate between "dark" and "bright" states do not change, as well as the relative zero field splitting. The valence state  $|v\rangle$  is not influenced by the presence of the defect (with and without localization), since no defect state is close to the valence state energy.

### EXCITON TRANSITION RATE

The dominant decay channel for excitons are optical transitions with rate

$$w = \tau^{-1} = \frac{\left( \omega_{i \rightarrow f}^3 |\vec{J} \cdot \langle \Psi_i | \hat{r} | \Psi_f \rangle \cdot q|^2 \right)}{3\pi\epsilon_0 c^3 \hbar}, \quad (\text{S4})$$

with  $|\Psi_f\rangle$  a valence wave function  $|v\rangle$ ,  $|\Psi_i\rangle$  is  $|c\rangle$  or  $|d\rangle$ ,  $\vec{J}$  the Jones vector and  $\omega_{i \rightarrow f} \hbar = \epsilon_i - \epsilon_f$ . Electron-phonon and electron scattering can be neglected as the experiments are performed at cryostatic temperatures and the density of accessible final states is low. We note that we treat the two-particle interaction perturbatively and therefore neglect the change of transition rates due to two-particle interactions. Furthermore, the considerations are restricted to

$\Gamma$  only and we do not consider any additional decay channels. Nevertheless we want to emphasize that relative transition rates between “bright” and “dark” excitons are expected to be captured by our model.

We calculate the position operator and subsequently the dipole transition rates via

$$\langle \phi_{i,\vec{R}} | \hat{r} | \phi_{j,0} \rangle = i \frac{\tilde{V}}{(s\pi)^3} \int d\vec{k} e^{i\vec{k}\cdot\vec{R}} \langle u_{i,\vec{k}} | \nabla_{\vec{k}} | u_{j,\vec{k}} \rangle \quad (\text{S5})$$

using the Wannier90 tool [S3, S4], where  $\phi_{i,\vec{R}}$  is the Wannier basis function with index  $i$  in the unit cell translated by  $\vec{R}$ . We extend Eq. (S5) to lattice site  $\vec{r}$  via the relation,

$$\langle \phi_{i,\vec{R}'} | \hat{r} | \phi_{j,\vec{R}} \rangle = \langle \phi_{i,\vec{R}'-\vec{R}} | \hat{r} | \phi_{j,0} \rangle + \delta_{\vec{R},\vec{R}'} \delta_{i,j} \vec{R}. \quad (\text{S6})$$

The approximation (S6) does not account for possible changes of the matrix element of  $\vec{r}$  due to inhomogeneous strain. The relative shifts to neighboring atoms - i.e. the dominant contributions to the position operator - are small and the strain influence as well as the defect relaxation are encoded in the wave functions. Therefore neglecting strain and defect relaxation still provides good estimates and correctly encodes information about valley and spin transition rates.

The optical oscillator strength can be interpreted in an “excited” exciton basis as the transition from an exciton state to the exciton ground state,

$$\langle 0, 0 | \hat{D}_{c \rightarrow v} | v, c \rangle = \langle \Psi_i | \hat{r} | \Psi_f \rangle \cdot q. \quad (\text{S7})$$

Under re-diagonalization, the dipole transitions of transformed exciton wave functions become

$$\langle 0, 0 | \hat{D} | \text{IDE} \rangle = \sum_{n \in \{\uparrow, \downarrow\}, m \in \{K, K'\}} \alpha_{n,m} \langle 0, 0 | \hat{D}_{n \rightarrow m} | d_n, v_m \rangle. \quad (\text{S8})$$

Therefore we obtain the dipole moment of the  $|\text{IDE}\rangle$  via a linear combination of the known excitonic transition rates of the defect excitons.

## TWO-PARTICLE INTERACTION

The direct  $W$  and indirect  $V$  part of the interaction kernel  $\Xi$  can be written in terms of the Coulomb operator as [S10]

$$W_{c_i, v_j}^{c_{i'}, v_{j'}} = \frac{1}{\varepsilon} \langle c_i, v_j | \hat{C}_{i,j}^{i',j'} | c_{i'}, v_{j'} \rangle \quad (\text{S9})$$

and

$$V_{c_i, v_j}^{c_{i'}, v_{j'}} = \langle c_i, v_j | \hat{C}_{j',j}^{i',i} | c_{i'}, v_{j'} \rangle. \quad (\text{S10})$$

The Coulomb operator  $\hat{C}$  in real space representation reads,

$$\hat{C}_{m,n}^{l,k} = \sum_{\vec{r}, \vec{r}'} \frac{\phi_m^\dagger(\vec{r}) \phi_n^\dagger(\vec{r}') \phi_l(\vec{r}) \phi_k(\vec{r}')}{|\vec{r} - \vec{r}'|} \quad (\text{S11})$$

with  $\phi_i(\vec{r}) = \langle \vec{r} | v_i(c_i) \rangle$  and  $s_i$  being the spin of state  $i$ . Note that the direct part is equivalent to the Hartree term in a single-particle description while the indirect part corresponds, but is not equivalent, to exchange in a single particle description.

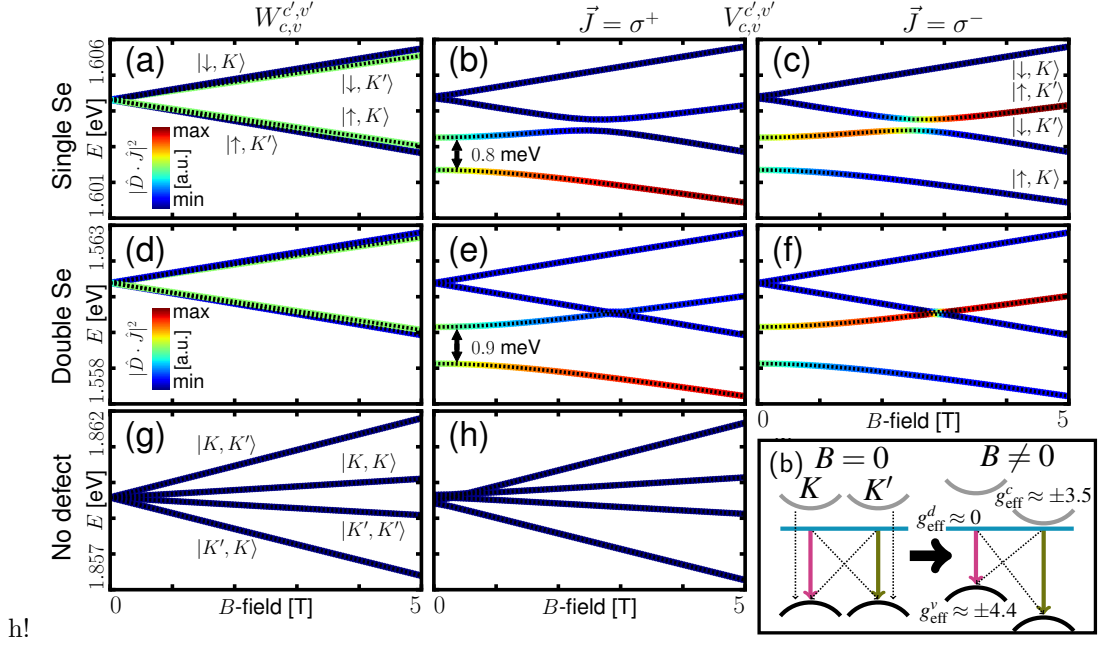


FIG. S4. Plotted for comparison. (a),(d) and (g) magnetic field splitting when only the direct contribution  $W$  is included. (a) for a single Se vacancy, (d) for a double Se vacancy and (g) for a defect free system. (b)-(c) splitting when also including the indirect contribution  $V$  for a single Se vacancy, (b) including right handed  $\sigma^+$  and (c) left handed  $\sigma^-$  light. When the symmetry in  $z$ -direction is broken by the single Se vacancy, an additional avoided crossing is observed. (e),(f) and (h) as in main text (see [Fig. S3]). (i) pictorial illustration of the process at  $B = 0$  and at  $B > 0$ . Cyan and brown arrows indicate allowed transitions, dashed lines indicate "dark" transitions. Half-circles indicate  $|v\rangle$  and  $|c\rangle$  states, the vertical line a defect state  $|d\rangle$ . The respective single particle effective  $g$ -factors are also shown.

### MAGNETIC FIELD CALCULATIONS FOR SINGLE SE VACANCY

Here we present the magnetic field dependent calculations of a single Selen vacancy. Since the single Se vacancy breaks the symmetry in  $z$  direction, an additional avoided crossing is observed near two Tesla where the lines cross for the double vacancy (see [Fig. S4 (a)-(c)]).

To underline the effects of the direct contribution  $W$  and the indirect contribution  $V$  to the magnetic field splitting we also show calculations including only the direct contribution (see [Fig. S4 (a), (d) and (g)]).

## COUPLED DOUBLETS

In the main text, we have given an approximate expression [Eq. (3)] for the localized inter-valley exciton  $|\text{IDE}_\pm\rangle$  in the limit where the hybridization with the conduction band is neglected on the BSE level. Considering now a stronger strain-induced mixture between conduction band  $|c\rangle$  and defect state  $|d\rangle$ , pairs of hybridized states  $|h\rangle_i$ ,  $i = 1, 2$  emerge on the single-particle level

$$|h\rangle_{1,\mathcal{S}} = \alpha(\mathcal{S})|d_0\rangle + \beta(\mathcal{S})|c_0\rangle \quad |h\rangle_{2,\mathcal{S}} = \beta(\mathcal{S})|d_0\rangle - \alpha(\mathcal{S})|c_0\rangle \quad (\text{S12})$$

with  $\alpha^2 + \beta^2 = 1$ ,  $\alpha(\mathcal{S} \rightarrow 0) = 1$ ,  $\beta(\mathcal{S} \rightarrow 0) = 0$ . Accordingly, the  $|\text{IDE}_\pm\rangle$  states evolve to the  $\mathcal{S} \rightarrow 0$  limit of one of two hybridization states

$$|\text{IDE}_\pm\rangle \approx \frac{1}{\sqrt{2}} \left( |d_{\uparrow(\downarrow)}v_{K(K')}\rangle \pm |d_{\downarrow(\uparrow)}v_{K'(K)}\rangle \right). \quad (\text{S13})$$

On the two-particle level, the hybridization is determined by the interplay between strain and the Coulomb interaction. Consequently, diagonalization of the full  $8 \times 8$  BSE Hamiltonian yields pairs of localized inter-valley exciton doublets,  $|\text{IDE}_\pm\rangle^{(1)}$  and  $|\text{IDE}_\pm\rangle^{(2)}$ , weakly coupled and energetically several meV apart. The resulting fine-structure of these coupled doublets reflect the mixture between defect excitonic  $|d, v\rangle$  and bulk excitonic  $|c, v\rangle$  states. Accordingly, the zero-field splitting which is due to the defect mode scales for the doublet  $|\text{IDE}_\pm\rangle^{(1)}$  as  $\Delta_1 \propto \alpha^2$  while for  $|\text{IDE}_\pm\rangle^{(2)}$  as  $\Delta_2 \propto \beta^2$  and will therefore decrease (increase) with the degree of hybridization. Similarly, the transition rate will depend on the relative weight of the defect admixture ( $\propto \alpha^2$  for  $|\text{IDE}_\pm\rangle^{(1)}$  and  $\propto \beta^2$  for  $|\text{IDE}_\pm\rangle^{(2)}$ ). The effective  $g$ -factors will be given by  $[g_{\text{eff}}]^{(1)} = g_{\text{eff}}^d \cdot \alpha^2 + g_{\text{eff}}^c \cdot \beta^2$  and  $[g_{\text{eff}}]^{(2)} = g_{\text{eff}}^d \cdot \beta^2 + g_{\text{eff}}^c \cdot \alpha^2$ , where  $g_{\text{eff}}^d = 8.8\mu_0$  and  $g_{\text{eff}}^c = 15.8\mu_0$  (see main text). We believe this dependence on the degree of hybridization explains the variations in  $g$ -factors of single photon emitters reported in the literature. Although understanding this fine-structure needs further careful investigation, these considerations show remarkable agreement with several experimental observations (e.g.  $\alpha = \beta$  [S27],  $\alpha < \beta$  [S17]).

## COMPARISON WITH EXPERIMENT

Using our multi-scale tight binding model, we calculate a range of properties of single-photon emitters. The Table S1 presents our key results and a comprehensive and concise comparison with experiment. We include a wide range of experimental results available from the literature. We find good agreement throughout. For observables such as the effective  $g$ -factor for perpendicular magnetic fields or Stark shifts, experiments yield a range of observed values that depend on the precise level of defect hybridization, alignment with the strain pattern, or symmetry breaking by the defect. Also for these cases, we provide insight into the expected possible range of values that is consistent with the spread found in the literature.

Observable	Our model	Experiment
Energy [eV]	<b>1.5-1.7</b>	<b>1.55-1.72</b> [S12–S21, S23–S28]
Lifetime [ns]	$\approx 1$	<b>0.5-8</b> [S13–S16, S19, S20, S23–S25, S27, S28] (0.1-0.5 Purcell enhanced) [S21]
Strain	<b>pillar 1-3%</b>	<b>pillar</b> [S25], <b>rails</b> [S19] measured [S13, S16, S20]
g-factor [ $\mu_0$ ]	<b>8.8</b>  (9-14)	<b>7.16</b> [S13], <b>8.7</b> [S14], <b>7.7-10.9</b> [S15], <b>6.3</b> [S21], <b>9-12</b> [S23], <b>9.8</b> [S24], <b>8</b> [S28] <b>9.4-10 (13)</b> [S17]
$\Delta_0$ [meV]	<b>0.8-2</b>	<b>0.7-0.9</b> [S13–S15, S20, S24, S26, S28], <b>1</b> [S18], <b>0.56</b> [S17], <b>0.2-0.4</b> [S16, S27], <b>0.2-0.73</b> [S25]
Polarization at $B = 0$ at $B > 5T$	<b>linear</b> <b>circular</b>	<b>linear</b> [S12–S14, S16–S20, S26, S27] <b>circular</b> [S14, S15, S17, S23]
Orientation doublets two singlets	<b>90</b> $\approx 0$	$\approx 90$ [S14, S17, S18, S26, S27], <b>40-90</b> [S13] <b>0</b> [S16, S27]
Stark shift linear [D] quadratic [ $\text{\AA}^3$ ]	<b>0.2 (0.1-10)</b> <b>2.1</b>	<b>0.058</b> [S18], <b>0.1-10</b> [S28] <b>1-1000</b> [S28] <b>3-98</b> [S22]
Coupled doublets		(see S VII.) ([S17, S27])

TAB. S1: Comparison of our model to various experimental results. Values in brackets are estimated (theory) or their origin is unclear (experiment).

- [S1] G. Kresse and J. Hafner, Phys. Rev. B, **47**, 558-561, (1993).  
[S2] G. Kresse and J. Hafner, Phys. Rev. B, **49**, 251-271, (1994).  
[S3] N. Marzari and D. Vanderbilt, Phys. Rev. B, **56**, 847-865, (1997).  
[S4] I. Souza, N. Marzari and D. Vanderbilt, Phys. Rev. B, **65**, 035109, (2001).  
[S5] S. Sanvito, PhD thesis, School of Physics and Chemistry, Lancaster University, Lancaster, LA1 4 YB, (1999).  
[S6] P. R. Amestoy, I. S. Duff, J. Koster, and J.-Y. L'Excellent, SIAM Journal of Matrix Analysis and Applications **23**, 15-41 (2001); P. R. Amestoy, A. Guermouche, J.-Y. L'Excellent and S. Pralet, Parallel Computing **32**, 136-156 (2006).  
[S7] K. J. Maschhoff and D. C. Sorensen. *P\_ARKPACK: An efficient portable large scale eigenvalue package for distributed memory parallel architectures*, volume 1184 (Applied Parallel Computing in Industrial Problems and Optimization) of *Lecture Notes in Computer Science*. Springer-Verlag, 1996. Editors: Jerzy Wasniewski, Jack Dongarra, Kaj Madsen, and Dorte Olesen.  
[S8] F. Libisch and J. Burgdörfer, PhD thesis, TU Vienna, (2012).  
[S9] N. Papior and M. Brandbyge, PhD thesis, TU Denmark, (2016).  
[S10] L. Reining, in, E. Pavarini, E. Koch, J. von den Brink and G. Sawatzky, ISBN 978-3-95806-159-0, Vol. **6**, (2016).  
[S11] K. He, N. Kumar, L. Zhao, Z. Wang, K. F. Mak, H. Zhao and J. Shan, Phys. Rev. Lett., **113**, 026803, (2014).  
[S12] P. Tonndorf, R. Schmidt, R. Schneider, J. Kern, M. Buscema, G. A. Steele, A. Castellanos-Gomez, H. S. J. van der Zant, S. Michaelis de Vasconcellos and R. Bratschitsch, Optica **2**, 347-352, (2015).  
[S13] S. Kumar, A. Kaczmarczyk, B. D. Gerardot, Nano Lett. **15**, 7567-7573, (2015).  
[S14] Y. He, G. Clark, J. R. Schaibley, Y. He, M. Chen, Y. Wei, X. Ding, Q. Zhang, W. Yao, X. Xu, C. Lu and J. Pan, Nature Nano. **10**, 497-502, (2015).  
[S15] A. Srivastava, M. Sidler, A. V. Allain, D. S. Lembke, A. Kis and A. Imamoglu, Nature Nano. **10**, 491-496, (2015).  
[S16] S. Kumar, M. Brotóns-Gisbert, R. Al-Khuzheyri, A. Branny, G. Ballesteros-Garcia, J. F. Sánchez-Royo and B. D. Gerardot, Optica **3**, 882-886, (2016).  
[S17] X. Lu, X. Chen, S. Dubey, Q. Yao, W. Li, X. Wang, Q. Xiong and A. Srivastava, Nature Nano., DOI:10.1038/s41565-019-0394-1, (2019).  
[S18] S. Schwarz, A. Kozikov, F. Withers, J.K. Maguire, A. P. Foster, S. Dufferwiel, L.Hague, M. N. Makhonin, L.R. Wilson, A. K. Geim, K. S. Novoselov and A. I. Tartakovskii, 2D Mater. **3**, 025038, (2016).  
[S19] J. Kern, I. Niehues, P. Tonndorf, R. Schmidt, D. Wigger, R. Schneider, T. Stiehm, S. Michaelis de Vasconcellos, D. E. Reiter, T. Kuhn and R. Bratschitsch, Adv. Mater. **28**, 7101-7105, (2016).  
[S20] A. Branny, S. Kumar, R. Proux and B. D. Gerardot, Nature Comm. **8**, 15053, (2017).

- [S21] Y. Luo, G. D. Shepard, J. V. Ardelean, D. A. Rhodes, B. Kim, K. Barmak, J. C. Hone and S. Strauf, *Nature Nano.* **13**, 1137-1142, (2018).
- [S22] C. Chakraborty, N. R. Jungwirth, G. D. Fuchs and A. N. Vamivakas, *Phys. Rev. B*, **99**, 045308, (2019).
- [S23] M. Koperski, K. Nogajewski, A. Arora, V. Cherez, P. Mallet, J.-Y. Veuillen, J. Marcus, P. Kossacki and M. Potemski, *Nature Nano.* **10**, 503-506, (2015).
- [S24] C. Chakraborty, L. Kinnischtzke, K. M. Goodfellow, R. Beams and A. N. Vamivakas, *Nature Nano.* **10**, 507-511, (2015).
- [S25] C. Palacios-Berraquero, D. M. Kara, A. R.-P. Montblanch, M. Barbone, P. Latawiec, D. Yoon, A. K. Ott, M. Loncar, A. C. Ferrari and M. Atatüre, *Nature Comm.* **8**, 15093, (2017).
- [S26] G. Clark, J. R. Schaibley, J. Ross, T. Taniguchi, K. Watanabe, J. R. Hendrickson, S. Mou, W. Yao and X. Xu, *Nano. Lett.* **16**, 3944-3948, (2016).
- [S27] Y. He, N. Lundt, V. Baumann, M. Davanco, K. Srinivasan, S. Höfling, C. Schneider, *Nature Comm.* **7**, 13409, (2016).
- [S28] C. Chakraborty, K. M. Goodfellow, S. Dhara, A. Yoshimura, V. Meunier and A. N. Vamivakas, *Nano. Lett.* **17**, 2253-2258, (2017).